

## GENERATION AND INTERACTION OF REVERSE AND NORMAL HAIRPIN VORTICES IN PIPE TRANSITION

**Shiyong Xiong**

State Key Laboratory for Turbulence and Complex Systems  
College of Engineering, Peking University  
Beijing 100871, China  
syxiong@pku.edu.cn

**Jiaping You**

State Key Laboratory for Turbulence and Complex Systems  
College of Engineering, Peking University  
Beijing 100871, China  
youjp@pku.edu.cn

**Shanxin Ruan**

State Key Laboratory for Turbulence and Complex Systems  
College of Engineering, Peking University  
Beijing 100871, China  
ruanshanxin@pku.edu.cn

**Yue Yang**

State Key Laboratory for Turbulence and Complex Systems  
College of Engineering, Peking University  
Beijing 100871, China  
yyg@pku.edu.cn

### ABSTRACT

We extend the vortex surface field (VSF), a Lagrangian-based structure-identification method, to the DNS database of a spatially developing pipe transition with the radial model inlet disturbance. The boundary-constraint method for constructing the VSF from an instantaneous vorticity field is adapted to pipe flows in cylindrical coordinates. The isosurfaces of the VSF, representing vortex surfaces consisting of vortex lines with different initial wall distances, display different evolutionary geometries in the transition. We observe that the near-wall vortex surface first forms a hairpin-like bulge, and then under the induction of the normal hairpin-like structure, some reverse hairpin-like structures grow from the core region of the pipe. The heads of normal and reverse hairpins approach to each other, leading to the strong vortex interaction and the formation of a turbulent spot. This process is quantified by the elevation and descend of two typical VSF isosurfaces initially near the wall and the core region, respectively.

### Introduction

The transition to turbulence in pipe flows is one of the most challenging problems in fluid mechanics over a centu-

ry (Reynolds, 1883) and is of importance in engineering applications such as drag reduction. The subcritical character of the pipe transition requires the disturbance with a finite magnitude to trigger transition process. Fundamental issues include the route to turbulence and the critical Reynolds number (Peixinho & Mullin, 2006; Eckhardt *et al.*, 2007; Schneider *et al.*, 2007; Mellibovsky *et al.*, 2009). The intermittent occurrence of turbulence in pipe transition manifests itself as puffs and slugs (Wynanski & Champagne, 1973; Song *et al.*, 2017). These localized structures expand in streamwise extent, decay and split, resulting in a finite life time around a critical Reynolds number (Hof *et al.*, 2006; Mullin, 2011). Some phenomenological models (Barkley, 2016) have been developed to characterize a bifurcation scenario at a macroscopic level to elucidate the origin of these localized structures. However, the pipe transition is still described as “abrupt and mysterious” (Mullin, 2011) without a detailed description of underlying flow physics.

This mystery can be partially resolved by the high-fidelity direct numerical simulation (DNS) of the spatially-developing transition in long pipes (Wu *et al.*, 2015). The DNS under circumferential-mode inlet disturbances revealed a gradual transition process and matured turbulent spots composed of primarily normal, forward leaning hair-

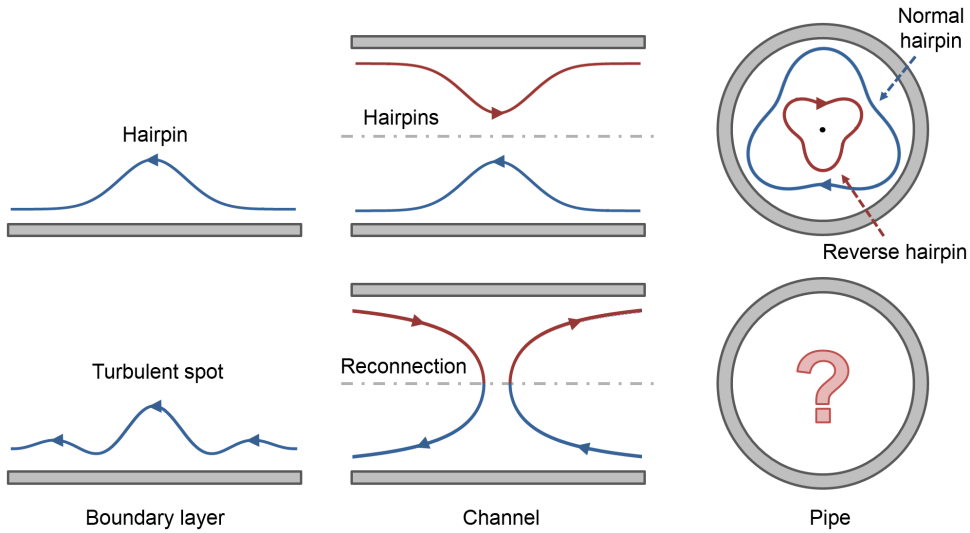


Figure 1. Schematic diagram (front view) of the evolution of vortex surfaces (from upper to lower panel) in transition in three canonical wall-bounded flows. Directions of vorticity tangent to the vortex surfaces are labeled by arrows.

pin vortices. On the other hand, it was recently reported that under radial-mode inlet disturbances, the turbulent spot composes primarily of reverse, backward leaning hairpin vortices (Adrian *et al.*, 2017), in direct contradiction to the earlier finding (Wu *et al.*, 2015). Moreover, the reverse hairpin vortices were also reported in the early studies on homogeneous turbulent shear flow (Rogers & Moin, 1987) and turbulent channel flow (Moin & Kim, 1985). However, there has been no thorough examination on the flow physics and quantitative criteria leading to the formation of reverse hairpin vortices, especially in spatially developing pipe transition.

The vortex-surface field (VSF) can be useful to uncover the flow physics and provide quantitative criteria for the generation of reverse and normal hairpin vortices in spatially-developing pipe transition. The VSF is developed for studying the Lagrangian-like evolution of vortical structures (Yang & Pullin, 2011). Every isosurface of the VSF is defined as a vortex surface consisting of vortex lines. The VSF has been applied to the Klebanoff-type transition in channel flow (Zhao *et al.*, 2016b) and boundary layer (Zhao *et al.*, 2018) to elucidate the continuous temporal evolution of vortical structures from a Lagrangian view and to quantify the connection between the deformation of VSFs and the rise of skin-friction.

The former VSF study demonstrated that the structural evolution of vortex surfaces in transition depends on the symmetry of flow boundary conditions. The schematic diagram of the evolution of vortex surfaces in transitions in three canonical wall-bounded flows is sketched in Fig. 1. The generation processes of hairpin-like bulges in transitional channel and boundary-layer flows are very similar, but their subsequent evolutions are essentially different. The channel flow has the symmetry in the wall-normal direction, so vortex surfaces can have reconnection between hairpin-like bulges elevated from opposite walls in transition (Zhao *et al.*, 2016b) and then the hairpin-like structures are destroyed. In contrast, this vortex reconnection does not occur in boundary-layer transition, and alternatively turbulent spots are generated owing to interactions of the structures in streamwise and spanwise directions (Zhao *et al.*, 2018). In pipe transition, the normal hairpins grown from

the wall and the reverse hairpins grown from the core region appear to converge to the bulk interlayer and lead to more complex vortex interactions than those in channel flows and boundary layers.

Therefore, we extend the VSF study to pipe transition. The continuous evolution of vortex surfaces from a Lagrangian perspective can shed light on the abrupt, mysterious transition process in pipe flows, and in particular, provide quantitative criteria for when and why reverse hairpins would appear and dominate.

## VSF method

The VSF construction can be considered as a post-processing step based on the given velocity fields obtained by DNS. The DNS of a spatially developing circular pipe with the radial mode inlet disturbance (Wu *et al.*, 2015; Adrian *et al.*, 2017) was carried out in cylindrical coordinates in a laboratory reference frame without the axially periodic boundary condition. The pipe length is  $500R$  with the pipe radius  $R$ , and the computational mesh size is  $16384 \times 200 \times 512$  in the axial ( $z$ ), radial ( $r$ ), and azimuthal ( $\theta$ ) directions, respectively. The parabolic laminar profile of the base flow is

$$U_z = U_m(1 - r^2), \quad (1)$$

with the maximum dimensionless velocity  $U_m = 2$  on the centerline. Finite-amplitude and localized radial-mode perturbations are introduced at the pipe inlet to induce gradual transition, eventually leading to a state of fully developed turbulence. No. 213 of the instantaneous DNS velocity data (Adrian *et al.*, 2017) is used in the present study by courtesy of Xiaohua Wu.

Given an instantaneous three-dimensional vorticity field  $\boldsymbol{\omega}(\mathbf{x}, t)$  at a time instant  $t$ , the VSF  $\phi_v$  is defined to satisfy the constraint (Yang & Pullin, 2010)

$$\mathcal{E}_v \equiv \boldsymbol{\omega} \cdot \nabla \phi_v = 0, \quad (2)$$

i.e., the vorticity vector is tangent to the isosurface of  $\phi_v$ , and every isosurface of  $\phi_v$  is a vortex surface consisting of vortex lines.

The boundary-constraint method (Xiong & Yang, 2017) for constructing the VSF from an instantaneous vorticity field has been adapted to pipe flows. The pseudo-transport equation with the VSF boundary constraint in the cylindrical coordinates  $(z, r, \theta)$  reads

$$\begin{cases} \frac{\partial \phi_v}{\partial \tau} + \omega_z \frac{\partial \phi_v}{\partial z} + \omega_r \frac{\partial \phi_v}{\partial r} + \frac{\omega_\theta}{r} \frac{\partial \phi_v}{\partial \theta} = 0, \\ \omega_z \frac{\partial \phi_v}{\partial z} + \omega_r \frac{\partial \phi_v}{\partial r} + \frac{\omega_\theta}{r} \frac{\partial \phi_v}{\partial \theta} = 0, \mathbf{x} \in \partial\Omega, \\ \phi_v = \phi_{v0}, \tau = 0, \end{cases} \quad (3)$$

where  $\Omega$  is the VSF computational domain,  $\tau$  is the pseudo-time variable defined to distinguish from the physical time  $t$ , and  $\omega_z$ ,  $\omega_r$ , and  $\omega_\theta$  are vorticity components in the stream-wise, radial, and azimuthal directions, respectively. Here, the VSF subzone of the entire DNS computational domain is selected as

$$\Omega = \{(z, r, \theta) | 10 < z/R < 25, -\pi/2 < \theta < \pi/2\} \quad (4)$$

to focus on the region with the emergence of coherent structures. The initial condition for Eq. (3) is set to  $\phi_{v0} = 1 - r/R$  and its isosurfaces are cylindrical surfaces, which stay invariant in the laminar Poiseuille flow. By solving Eq. (3), the given initial condition  $\phi_{v0}$  converges to an approximate VSF solution.

In the numerical implementation, Eq. (3) is advanced in  $\tau$  using the third-order total-variation diminishing Runge-Kutta method, and the convection term is treated by the fifth-order weighted essentially nonoscillatory (WENO) scheme. The numerical diffusion in the WENO scheme can serve as a numerical dissipative regularization for Eq. (3). In order to increase the computational accuracy and efficiency in the calculation of Eq. (3), two ghost zones are added next to the azimuthal boundaries, in which vortex lines are stretched to be normal to boundaries of the ghost zones. More details of the boundary-constraint method can be found in Xiong & Yang (2017).

In general, the computed  $\phi_v$  cannot be an exact VSF solution, and the deviation of isosurfaces of  $\phi_v$  from vortex surfaces is quantified by the cosine of the angle between the vorticity  $\boldsymbol{\omega}$  and the scalar gradient  $\nabla\phi_v$  as  $\lambda_\omega \equiv \boldsymbol{\omega} \cdot \nabla\phi_v / (|\boldsymbol{\omega}| |\nabla\phi_v|)$  (Yang & Pullin, 2010). The numerical VSF solution is calculated on uniform grid points  $N_z^\phi = 1500$ ,  $N_r^\phi = 500$ , and  $N_\theta^\phi = 500$ , with vorticity  $\boldsymbol{\omega}$  interpolated onto the grid points in  $\Omega$  for VSF calculation. The pseudo evolution of the averaged  $\lambda_\omega$  is shown in Fig. 2, where  $\langle \cdot \rangle$  denotes the volume average over  $\Omega$ . Since the deviation is around 1%, the boundary-constraint method can provide a very accurate VSF in the transitional pipe flow.

## Results

To characterize the transition process, we calculate an energy norm of the fluctuating velocity in  $\Omega$  as

$$E = \frac{\int_0^{2\pi} \int_0^R (u_z^2 + u_r^2 + u_\theta^2) r dr d\theta}{\int_0^{2\pi} \int_0^R U_z^2 r dr d\theta} \quad (5)$$

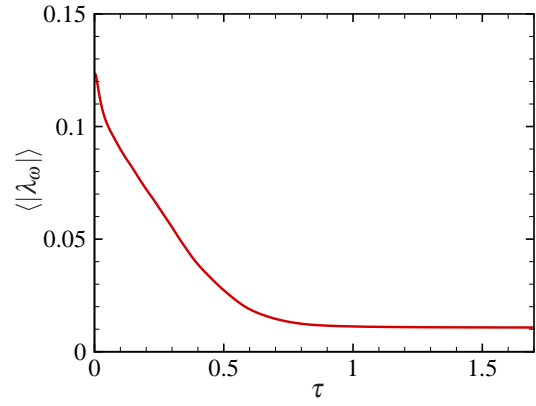


Figure 2. Pseudo-evolution of  $\langle |\lambda_\omega| \rangle$  in the VSF computational domain.

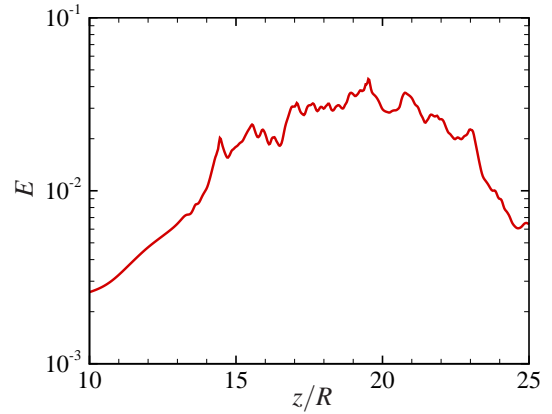


Figure 3. Spatial evolution of the energy norm of the fluctuating velocity in the axial direction.

where  $u_z$ ,  $u_r$ , and  $u_\theta$  are fluctuating velocity components in axial, radial, and azimuthal directions, respectively. As shown in Fig. 3, the energy norm in the instantaneous DNS velocity data grows exponentially with the axial distance from  $z/R = 10$  to 15, then fluctuates from  $z/R = 15$  to 22 and peaks around  $z/R = 20$ , and finally decays. Correspondingly, from the isosurface of the swirling strength  $\lambda_{ci}$  in Fig. 4, small-scale hairpin-like structures abruptly emerge and subsequently grow into a ‘turbulent spot’ comprised of a number of hairpin-like structures, then the flow is re-laminarized with vanishing hairpin-like structures.

We use VSF isosurfaces to characterize the interaction between the normal and reverse hairpin vortices in the pipe transition. The isosurfaces with the same initial cylindrical geometry and different initial wall-distances can have different geometries in their evolution. The VSF isosurfaces constructed from the instantaneous DNS database of pipe transition at  $10 < z/R < 25$  in  $\Omega$  are shown in Fig. 4. The inner VSF isosurface of  $\phi_v = 0.6$  initially near the central core region is color-coded by the normalized radial coordinate  $r/R$ , and the outer VSF isosurface of  $\phi_v = 0.2$  initially near the wall is translucent and colored in gray. In Fig. 4, the vortex surface near the wall first forms a thumb-shaped bulge and then evolves into a hairpin-like structure, which is very similar to the channel flow transition (Zhao *et al.*, 2016b) and the boundary-layer transition (Zhao *et al.*, 2018). Subsequently, under the induction of these normal hairpin vortices which generates the fluc-

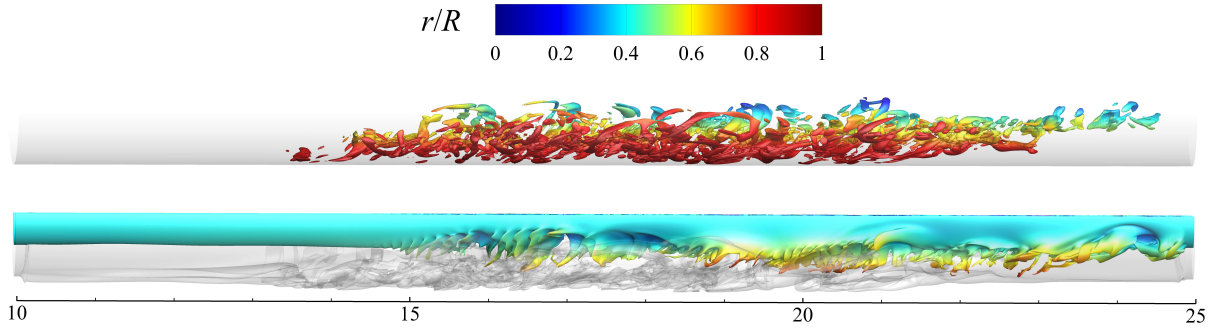


Figure 4. The side view of isosurfaces of  $\lambda_{ci}$  (top) and VSF (bottom) constructed from the DNS of pipe transition at  $10 < z/R < 25$ . The isosurface of  $\lambda_{ci}$  and the inner VSF isosurface of  $\phi_v = 0.6$  near the core region is color-coded by the normalized radial coordinate  $r/R$ , and the outer VSF isosurface of  $\phi_v = 0.2$  near the wall is translucent and colored in gray.

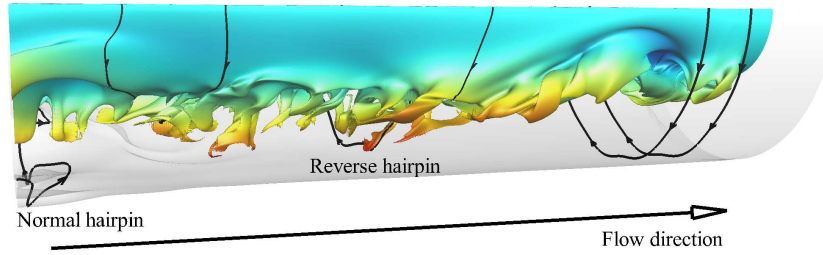


Figure 5. The zoomed-in, perspective view of VSF isosurfaces around  $21 < z/R < 25$  extracted from Fig. 4. Some vortex lines are integrated from the surfaces.

tuating wall-normal velocity, some reverse hairpin vortices grow from the core region of the pipe. The interaction of these reverse hairpins among themselves or with the normal hairpins produces small-scale hairpin packets, which leads to the formation of a turbulent spot around  $z/R = 20$ . These observations display a gradual and continuous evolution of vortex surfaces during the transition process. By contrast, the emergence and disappearance of coherent structures visualized by the isosurface of Eulerian vortex-identification criteria (e.g.,  $\lambda_{ci}$ ) appear to be abrupt without enough clues for explaining the structural change.

In particular, we elucidate the generation mechanism of reverse hairpin vortices in pipe transition with radial inlet disturbances using VSF. As shown in the close-up view of VSF isosurfaces at  $21 < z/R < 25$  in Fig. 5, all the vortex lines are closed loops in the background Poiseuille flow. If they are perturbed in the radial direction, the vortex surfaces near the core region can be pulled down and gradually deform under the shear layer. Subsequently they form reverse triangular bulges and hairpin-like structures, and descend to the wall. Their “heads” with larger  $r$  move slower than their “legs” with smaller  $r$  so that the legs are stretched. This mechanism is similar to the formation of normal hairpins generated from the wall (Zhao *et al.*, 2016b, 2018), but the two types of hairpins generally have opposite preferential orientations (see Fig. 1).

To further quantify the VSF results, we choose two typical VSF isosurfaces to characterize the elevation and descent of vortex surfaces along the streamwise direction. For a given VSF isosurface at a given  $z$ , the distance to the wall of sample points  $G = \{(z_i, r_i, \theta_i)\} | i \in \{0, 1, \dots, N_G\}$  on this

surface is calculated as

$$d_r(\phi_v, z) = 1 - r(\phi_v, z), \quad (6)$$

and we define operators of averaging, maximum, and minimum of  $d_r$  over the azimuthal direction by  $\langle \cdot \rangle_\theta$ ,  $\max_\theta(\cdot)$ , and  $\min_\theta(\cdot)$ , respectively.

Figure 6 plots the wall distances of VSF isosurfaces of  $\phi_v = 0.2$  and  $0.6$ . We observe that the mean wall distance  $\langle d_r \rangle_\theta$  of these two VSF isosurfaces remains almost unchanged, owing to the quasi-conservation of mass between a vortex surface and the wall (Zhao *et al.*, 2016a). On the other hand, the leading edge of the normal hairpin is generated and lifted from the wall, as the growth of  $\max_\theta(d_r)$  for  $\phi_v = 0.2$  in Fig. 6, and then the descended reverse hairpins forms around the core and grows to the wall near  $z/R = 16$ , as the decrease of  $\min_\theta(d_r)$  for  $\phi_v = 0.6$ . Figure 7 plots contour lines of  $\phi_v = 0.2$  and  $0.6$  on the  $z$ - $r$  plane to further illustrate the generation of the normal and reverse hairpins. Around  $z/R = 20$ , the reverse hairpins interact with the normal hairpins, leading to the formation of a turbulent spot. The event of approaching vortex surfaces from the wall and the core region coincides with the growth of the energy norm of fluctuating velocity in Fig. 3. Finally around  $z/R = 25$ , both  $\max_\theta(d_r)$  and  $\min_\theta(d_r)$  converge to their  $\langle d_r \rangle_\theta$ , indicating that VSF isosurfaces are relaxed towards cylindrical surfaces and the flow is re-laminarized.

As sketched in Fig. 1, the interaction of vortex surfaces in pipe transition is very different from transitions of channel flow and boundary-layer flow owing to different symmetries of boundary conditions. Figure 8 plots the

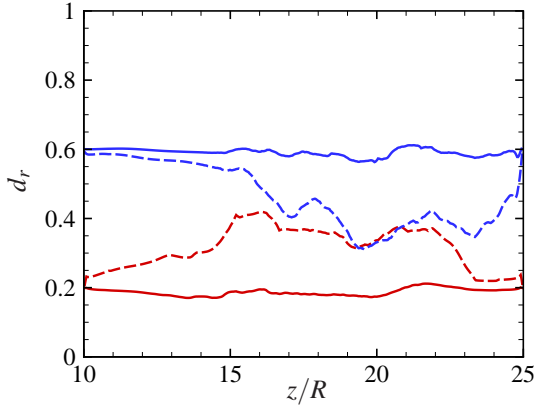


Figure 6. Wall distances of two typical VSF isosurfaces. Solid blue line:  $\langle d_r \rangle_\theta$  for  $\phi_v = 0.6$ , dashed blue line:  $\min_\theta(d_r)$  for  $\phi_v = 0.6$ , solid red line:  $\langle d_r \rangle_\theta$  for  $\phi_v = 0.2$ , dashed red line:  $\max_\theta(d_r)$  for  $\phi_v = 0.2$ .

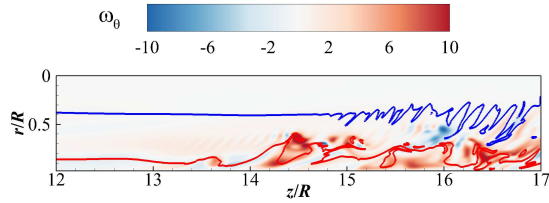


Figure 7. VSF contour lines of  $\phi_v = 0.6$  (blue) and  $\phi_v = 0.2$  (red) on the  $z$ - $r$  plane with the contour of  $\omega_\theta$  at  $12 \leq z/R \leq 17$ .

VSF contour lines on  $r$ - $\theta$  planes with contours of streamwise vorticity at four streamwise locations. At  $z/R = 11$  in Fig. 8(a), under the inlet disturbance, the VSF contour line of  $\phi_v = 0.2$  near the wall is deformed to form some bulges. These near-wall bulges develop further downstream at  $z/R = 15$  in Fig. 8(b) and induce deformation of the VSF contour line of  $\phi_v = 0.6$  near the core region. The two VSF contour lines continue to deform and gradually approach to each other at  $z/R = 20$  in Fig. 8(c). In particular, the nearly parallel directions of vortex lines of normal and reverse hairpin heads in Fig. 9 induce stronger vortex interactions with intensive vorticity amplification (Xiong & Yang, 2019) than the viscous calculation of approaching nearly anti-parallel vortex lines in the transition of channel flows (Zhao *et al.*, 2016b). Moreover, the background contour shows that the strong positive and negative streamwise vorticities appear in pairs, which is due to the deformed VSF contour lines are extended towards the streamwise direction to form hairpin legs. Finally, the flow field becomes re-laminarized, and VSF contour line of  $\phi_v = 0.2$  near the wall at  $z/R = 24$  in Fig. 8(d) relaxes to the initial ring.

## Conclusions

The VSF is applied to the DNS database of a spatially developing circular pipe with the radial model inlet disturbance. In order to construct the VSF from an instantaneous vorticity field in pipe flow, the boundary-constraint method (Xiong & Yang, 2017) is adapted to cylindrical coordinates.

Isosurfaces of the VSF are extracted to visualize the continuous evolution of vortex surfaces, which elucidates

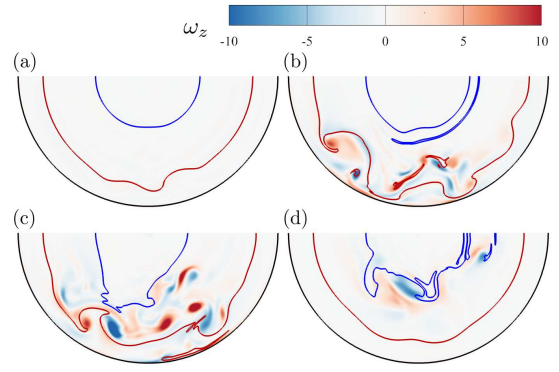


Figure 8. VSF contour lines of  $\phi_v = 0.6$  (blue) and  $\phi_v = 0.2$  (red) on the  $r$ - $\theta$  plane with the contour of  $\omega_z$  at (a)  $z/R = 11$ , (b)  $z/R = 15$ , (c)  $z/R = 20$ , and (d)  $z/R = 24$ .

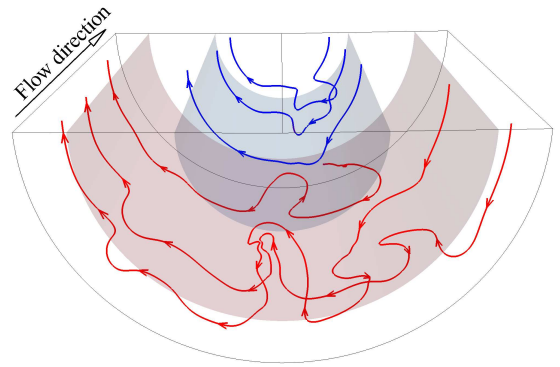


Figure 9. The front view of typical vortex lines integrated on VSF isosurfaces of  $\phi_v = 0.6$  (blue lines) and  $\phi_v = 0.2$  (red lines) at  $12 \leq z/R \leq 17$ . The translucent surfaces denote initial VSF isosurfaces of  $\phi_{v,0} = 0.6$  (blue) and  $\phi_{v,0} = 0.2$  (red).

the abrupt generation and interaction of reverse and normal hairpin vortices in pipe transition. The VSF isosurfaces, with the same initial cylindrical geometry and different initial wall distances, show different evolutionary geometries in the transition. We observe that the VSF isosurface near the wall first forms a thumb-shaped bulge and develops into a hairpin-like structure. Subsequently under the induction of these normal hairpin vortices, some reverse hairpin vortices grow from the core region of the pipe. The strong interaction of the normal and reverse hairpins or among themselves produces small-scale structures, leading to the formation of a turbulent spot. This event coincides with the growth of the energy norm of fluctuating velocity, and is quantified by the elevation and descent of two VSF isosurfaces initially near the wall and the core region, respectively. Then, VSF isosurfaces are relaxed towards initial cylindrical surfaces and the flow is re-laminarized.

Based on the VSF study of pipe transition and former VSF studies of transitional channel and boundary-layer flows (Zhao *et al.*, 2016b, 2018), we will compare different dynamics of vortex surfaces and explore whether universal flow structures or processes exist in transition in three canonical wall-bounded flows. The similarities in structural evolution in transitional flows can be helpful to develop

more universal subgrid-scale wall models and data-driven predictive tools in wall-bounded flows.

## REFERENCES

- Adrian, R., Wu, X. & Moin, P. 2017 Turbulent spots and scalar flashes in pipe transition. In *70th Annual Meeting of the American Physical Society, Division of Fluid Dynamics*. Denver, CO, USA.
- Barkley, D. 2016 Theoretical perspective on the route to turbulence in a pipe. *J. Fluid Mech.* **803**, P1.
- Eckhardt, B., Schneider, T. M., Hof, B. & Westerweel, J. 2007 Turbulence transition in pipe flow. *Annu. Rev. Fluid Mech.* **39**, 447–468.
- Hof, B., Westerweel, J., Schneider, T. M. & Eckhardt, B. 2006 Finite lifetime of turbulence in shear flows. *Nature* **443**, 59–62.
- Mellibovsky, F., Meseguer, Á., Schneider, T. M. & Eckhardt, B. 2009 Transition in localized pipe flow turbulence. *Phys. Rev. Lett.* **103**, 054502.
- Moin, P. & Kim, J. 1985 The structure of the vorticity field in turbulent channel flow. Part 1. Analysis of instantaneous fields and statistical correlations. *J. Fluid Mech.* **155**, 441–464.
- Mullin, T. 2011 Experimental studies of transition to turbulence in a pipe. *Annu. Rev. Fluid Mech.* **43**, 1–24.
- Peixinho, J. & Mullin, T. 2006 Decay of turbulence in pipe flow. *Phys. Rev. Lett.* **96**, 094501.
- Reynolds, O. 1883 An experimental investigation of the circumstances which determine whether the motion of water shall be direct or sinuous, and of the law of resistance in parallel channels. *Philos. Trans. R. Soc. A* **174**, 935–982.
- Rogers, M. M. & Moin, P. 1987 The structure of the vorticity field in homogeneous turbulent flows. *J. Fluid Mech.* **176**, 33–66.
- Schneider, T. M., Eckhardt, B. & Yorke, J. A. 2007 Turbulence transition and the edge of chaos in pipe flow. *Phys. Rev. Lett.* **99**, 034502.
- Song, B., Barkley, D., Hof, B. & Avila, M. 2017 Speed and structure of turbulent fronts in pipe flow. *J. Fluid Mech.* **813**, 1045–1059.
- Wu, X., Moin, P., Adrian, R. J. & Baltzer, J. R. 2015 Osborne Reynolds pipe flow: Direct simulation from laminar through gradual transition to fully developed turbulence. *Proc. Natl. Acad. Sci.* **112**, 7920–7924.
- Wynagnanski, I. J. & Champagne, F. H. 1973 On transition in a pipe. part 1. the origin of puffs and slugs and the flow in a turbulent slug. *J. Fluid Mech.* **59**, 281–335.
- Xiong, S. & Yang, Y. 2017 The boundary-constraint method for constructing vortex-surface fields. *J. Comput. Phys.* **339**, 31–45.
- Xiong, S. & Yang, Y. 2019 Evolution and helicity analysis of linked vortex rings in viscous flows. *Sci. Sinica Phys. Mech. Astro.* DOI: 10.1360/SSPMA-2019-00922019 (in Chinese).
- Yang, Y. & Pullin, D. I. 2010 On Lagrangian and vortex-surface fields for flows with Taylor–Green and Kida–Pelz initial conditions. *J. Fluid Mech.* **661**, 446–481.
- Yang, Y. & Pullin, D. I. 2011 Evolution of vortex-surface fields in viscous Taylor–Green and Kida–Pelz flows. *J. Fluid Mech.* **685**, 146–164.
- Zhao, Y., Xiong, S., Yang, Y. & Chen, S. 2018 Sinuous distortion of vortex surfaces in the lateral growth of turbulent spots. *Phys. Rev. Fluids* **3**, 074701.
- Zhao, Y., Yang, Y. & Chen, S. 2016a Evolution of material surfaces in the temporal transition in channel flow. *J. Fluid Mech.* **793**, 840–876.
- Zhao, Y., Yang, Y. & Chen, S. 2016b Vortex reconnection in the late transition in channel flow. *J. Fluid Mech.* **802**, R4.